PSR B0329+54: SUBSTRUCTURE IN THE SCATTER-BROADENED IMAGE DISCOVERED WITH RADIOASTRON ON BASELINES OF UP TO 235,000 KM

M. V. Popov[1], A. S. Andrianov[1], N. Bartel[2], C. R. Gwinn[3], M. D. Johnson[4], B. C. Joshi[5], N. S. Kardashev[1], R. Karuppusamy[6], Y. Y. Kovalev[1,6], M. Kramer[6], A. G. Rudnitskii[1], E. R. Safutdinov[1], V. I. Shishov[7], T. V. Smirnova[7], V. A. Soglasnov[1], J. A. Zensus[6], V. I. Zhuravlev[1]

ABSTRACT

We studied scattering properties of the pulsar PSR B0329+54 with a ground-space radio interferometer *RadioAstron* which included the 10-m Space Radio Telescope, the 110-m Green Bank Telescope, the 14×25-m Westerbork Synthesis Radio Telescope, and the 64-m Kalyazin Radio Telescope. The observations were performed at 324 MHz on baselines of up to 235,000 km in November 2012 and January 2014. At short ground-space baselines of less than about 20,000 km, the visibility amplitude decreases with the projected baseline length, providing a direct measurement of the diameter of the scattering disk of 4.7 ± 0.9 mas. The size of the diffraction spot near Earth is $15,000 \pm 3,000$ km. At longer baselines of up to 235,000 km, where no interferometric detection of the scattering disk would be expected, significant visibilities were observed with amplitudes scattered around a constant value. These detections result in a discovery of a substructure in the completely resolved scatter-broadened image of the pointlike source, PSR B0329+54. They fully attribute to properties of the interstellar medium. The visibility function at the longest ground-space baselines in the delay domain consists of many isolated unresolved spikes, in agreement with the amplitude-modulated noise model. Within the assumption of turbulent as well as large-scale irregularities in the plasma of the interstellar medium, we estimate that the effective scattering screen lies 0.35 ± 0.10 of the distance from Earth toward the pulsar.

Subject headings: scattering — pulsars: individual B0329+54 — radio continuum: ISM — techniques: high angular resolution

1. INTRODUCTION

All radio signals from cosmic sources are distorted by the plasma turbulence in the interstellar medium (ISM). Understanding of this turbulence is therefore essential for the proper interpretation of astronomical radio observations. The properties and characteristics of this turbulence can best be studied by observing point-like radio sources, where the results are not influenced by the extended structure of the source, but instead directly attributed to the effect of the ISM itself. Pulsars are such sources. The propagation of pulsar radio emission through the ISM is accompanied by dispersion, and scattering by inhomogeneities in the plasma. While the dispersion causes delay in arrival time at different frequencies and consequent pulse smearing, the scattering causes angular broadening, pulse broadening, intensity modulation or scintillation, and distortion of radio spectra in the form of diffraction patterns. The scattering effects have already been studied extensively theoretically (see, e.g., Prokhorov et al. 1975; Rickett 1977; Goodman & Narayan 1989; Narayan & Goodman 1989; Gwinn et al. 1998; Shishov et al. 2003), observationally with

ground VLBI of Sgr A* (Gwinn et al. 2014) and pulsars (see, e.g., Kondratiev et al. 2007; Gwinn et al. 1993; Desai et al. 1992; Bartel et al. 1985) as well as ground-space VLBI of PSR B0329+54 (VSOP, Yangalov et al. 2001). However, whereas the latter observations were done at a relatively high frequency of 1.7 GHz and with baselines only up to about 25,000 km, ground-space VLBI with *RadioAstron* allowed observations at one-fifth the frequency where propagation effects are expected to be much stronger, and with baselines ~ 10 times longer. With such observations the scatter-broadened image of a pulsar could perhaps be resolved and characteristics of the propagation medium revealed. Here we investigate scattering effects with *RadioAstron* (Kardashev et al. 2013).

PSR B0329+54 is the strongest pulsar in the northern hemisphere. It is located at a Galactic longitude of $145°$ and latitude of $-1°.2$, and at a parallax distance of $1.03^{+0.13}_{-0.12}$ kpc (Brisken et al. 2002), just at the outer edge of the Orion spiral arm. The VSOP observations did not resolve the scattering disk and resulted only in an upper limit of the angular size of $\theta_{\rm scat} < 2$ mas (Yangalov et al. 2001). Since the scattering size increases as λ^2, this upper limit corresponds to a size of < 50 mas at 327 MHz. *RadioAstron* has at this frequency an angular resolution of up to about 1 mas, and therefore a new attempt to resolve PSR B0329+54's scattering disk and perhaps reveal hitherto unknown structure in the ISM appeared to be promising.

2. OBSERVATIONS

The observations were made in two sessions: the first for one hour each on the four successive days November 26 to 29, 2012, and the second for a total of 12 hours on the two days January 1 and 2, 2014. The first session used the 10-

[1] Lebedev Physical Institute, Astro Space Center, Profsoyuznaya 84/32, Moscow 117997 Russia; yyk@asc.rssi.ru

[2] York University, 4700 Keele St., Toronto, ON M3J 1P3, Canada

[3] University of California at Santa Barbara, Santa Barbara, CA 93106-4030, USA

[4] Harvard-Smithsonian Center for Astrophysics, 60 Garden St, Cambridge, MA 02138, USA

[5] National Centre for Radio Astrophysics, Post Bag 3, Ganeshkhind, Pune 411007 India

[6] Max-Planck Institut für Radioastronomie, Auf dem Hügel 69, Bonn 53121, Germany

[7] Lebedev Physical Institute, Pushchino Radio Astronomy Observatory, Pushchino 142290, Moscow region, Russia

m *RadioAstron* Space Radio Telescope (SRT) together with the 110-m Robert C. Byrd Green Bank Telescope (GBT). The second session used the SRT together with the 14×25-m Westerbork Synthesis Radio Telescope (WSRT) and the 64-m Kalyazin Radio Telescopes (KL). Both right (RCP) and left circular polarizations (LCP) were recorded in November 2012, and only one polarization channel (RCP) was recorded in January 2014. Because of an SRT peculiarity at 324 MHz, only the upper sideband of the 316–332 MHz observing band was recorded, with one-bit digitization at the SRT and with two-bit digitization at the GBT, WSRT, and KL. Science data from the SRT were transmitted in real time to the telemetry station in Pushchino (Alexandrov et al. 2012) and then recorded with the *RadioAstron* data recorder (RDR). This type of recorder was also used at the KL, while the Mk5B recording system was used at the GBT and WSRT.

The data were transferred via internet to the Astro Space Center (ASC) in Moscow and then processed with the ASC correlator with gating and dedispersion applied. To determine the phase of the gate in the pulsar period, the average pulse profile was computed for every station by integrating the auto-correlation spectra (auto-spectra) obtained from the ASC correlator.

The amplitudes of the average pulse profiles allowed us to accurately determine the sensitivities of each of the radio telescopes, including the SRT. On empty sky the GBT system temperature is known to be $T_{sys}^{GBT} = 90$ K and the system equivalent flux density $SEFD^{GBT} = 45$ Jy at $\nu = 324$ MHz. The sky temperature in the direction of the pulsar at a frequency $\nu = 408$ MHz is $T_{sky} = 56$ K (Haslam et al. 1982). With a spectral index $\alpha = -2.5$ and flux density $S_\nu \propto \nu^\alpha$, we estimate $T_{sky} = 100$ K at $\nu = 324$ MHz. This corresponds to an extra 50 Jy for the SEFD. Therefore, the total SEFD for the GBT in the pulsar direction is $SEFD_{psr}^{GBT} = 95$ Jy. The peak flux density of the pulsar in a selected scan was $\Delta S / SEFD_{psr}^{GBT} = 3.33$ times larger, or $\Delta S = 325$ Jy. For the SRT and the same scan $\Delta S / SEFD_{psr}^{SRT}$ was found to be 0.008. After correction for the one-bit sampling factor of 1.57, this ratio becomes 0.0125, yielding $SEFD_{psr}^{SRT} = 26,000$ Jy. This value is somewhat in excess of the $SEFD^{SRT} = 19,000$ Jy measured for the SRT in the total power mode in space (Kovalev et al. 2014). Similar computations give $SEFD_{psr}^{WSRT} = 255$ Jy and $SEFD_{psr}^{KL} = 650$ Jy for the WSRT and KL, respectively.

In November 2012 the baseline projections were about 60, 90, 175, and 235 thousand kilometers for the four consecutive days, respectively. Data were recorded in 570-second scans, with 30-second gaps between scans. In January 2014 the baseline projections were about 20, 70, and 90 thousand kilometers during the 12-hour session. Data were recorded in 1170-second scans. The SRT operated only during three sets of scans of 60, 100 and 120 min each, with large gaps in between caused by thermal constraints on the spacecraft. The auto-level (AGC), phase cal, and noise diode were turned off during our observations to avoid interference with pulses from the pulsar.

3. DATA REDUCTION

All data obtained were correlated with the ASC correlator using 4096 channels for the November 2012 session and 2048 channels for the January 2014 session, with gating and dedispersion activated. The ON-pulse window was centered on the main component of the average profile, with a width of 5 ms in the November 2012 session and 8 ms in the January 2014 session. The OFF-pulse window was offset from the main pulse by half a period and had the same width as the ON-pulse window. The correlator output was sampled synchronously with the pulsar period of 0.714 s (single pulse mode). We used ephemerides computed with the program TEMPO for the Earth center (Edwards et al. 2006). The results of the correlation were tabulated as cross-correlation spectra (cross-spectra) written in standard FITS format.

For the subsequent analysis we used the CFITSIO package (Pence 1999). We calibrated the data in seven steps. First, we corrected for strong narrow-band interference by replacing the affected data with properly scaled random numbers. Second, we applied corrections for the SRT and GBT receiver bandpasses using OFF-pulse cross-spectra as templates. Third, we reduced the influence of strong pulse-to-pulse intensity fluctuations by normalizing the cross-spectra according to the pulse intensities obtained from auto-spectra at the GBT, WSRT, and KL, where single pulses were easily seen. The normalization factor, R_{cor}, is computed as:

$$R_{cor}^{-1} = \sqrt{(\sigma_{1on}^2 - \sigma_{1off}^2)(\sigma_{2on}^2 - \sigma_{2off}^2)} \qquad (1)$$

Here, σ_{1on}^2 and σ_{1off}^2 are the variances for the pulses observed at the ground radio telescope used for cross-correlation, computed in ON-pulse and OFF-pulse windows as the sum of all harmonics in the power auto-spectra. Similarly, σ_{2on}^2 and σ_{2off}^2 are the variances for the SRT spectra, computed in the same way. Fourth, since the values of σ_{off} were slowly varying because we had the AGC system switched off, we used a polynomial approximation for σ_{off} at each of the telescopes computed in advance. Fifth, the relatively low sensitivity of the SRT renders the measurement of $\sigma_{2on}^2 - \sigma_{2off}^2$ rather uncertain. It can even give negative values. We therefore replaced the value of this difference with the ON-pulse intensity for a given ground radio telescope (GRT), but reduced to the expected value for the SRT using the coefficient $\eta = SEFD_{GRT}/SEFD_{SRT}$. This coefficient was taken to be equal to 0.0024, 0.0063, and 0.016 for the GBT, WSRT and KL, respectively, which, with the sampling factor taken into account, corresponds to the ratios of the SEFD values given in § 2. Then, equation 1 can be written as:

$$R_{cor}^{-1} = \frac{\sigma_{2off}}{\sigma_{1off}}(\sigma_{1on}^2 - \sigma_{1off}^2)\sqrt{\eta} \qquad (2)$$

Sixth, we normalized the cross-spectra according to equation 2. For the November 2012 spectrum, when we averaged cross-spectra by 10 pulses, we normalized every pulse, but only accepted cross-spectra of strong pulses: that is, pulses for which the sum of the harmonics of the ON-pulse auto-spectra was larger than 6 times the rms of the OFF-pulse intensity fluctuations. For the January 2014 observing session, we also normalized every cross-spectrum, but if the normalization factor was greater than 20 we left the spectrum unnormalized to avoid strong amplification of noise. For this later session, we left the data in single-pulse form for further analysis.

Seventh, for the November 2012 session only, we improved the signal-to-noise ratio (SNR) through averaging. An analysis of the dynamic auto-spectra of the GBT data for the November 2012 session showed the diffraction scintillation time to be $t_{diff} = 114 \pm 2$ s, and the scintillation bandwidth to be $\Delta\nu_{diff} = 15 \pm 2$ kHz. We averaged the complex cross-spectra over 10 pulsar periods, resulting in a sampling period

TABLE 1
PSR B0329+54 SCATTERING PARAMETERS

Epoch	t_{diff} (s)	$\Delta\nu_{\mathrm{diff}}$ (kHz)	$w_{n\tau}$ (ns)	w_{nf} (mHz)	$w_{b\tau}$ (μs)
(1)	(2)	(3)	(4)	(5)	(6)
November 2012	114 ± 2	15 ± 2	50 ± 5	2.6 ± 0.1	5.1 ± 0.2
January 2014	102 ± 2	7 ± 2	43 ± 3	3.0 ± 0.1	7.5 ± 0.2

NOTE. — Columns are as follows: (1) date of observations, (2) diffraction scintillation time obtained from the dynamic autocorrelation spectra at the GBT as the half width at 1/e of the maximum of the broad component, (3) scintillation bandwidth obtained from the spectra at the GBT as the half-width at half maximum (HWHM), (4) HWHM of a sinc function fit to the central spike of the visibility amplitude distribution along the delay axis, (5) HWHM of a sinc function fit to the central spike of the visibility amplitude distribution along the fringe rate axis, (6) HWHM of a Lorentzian fit to the broad component of the visibility amplitude distribution along the delay axis, whic is the scattering time broadening.

of 7.14 s. In rare cases, when none of the 10 cross-spectra in an averaging period met this condition, the previous cross-spectrum was taken for this averaging period instead. In every observing scan, 570 s long, we took a round number of 70 normalized and averaged cross-spectra. These cross-spectra were used for further analysis.

The initial averaging time, Δt_{int}, was smaller than t_{diff}, and our channel bandwidths, $\Delta\nu_{\mathrm{int}} = 16$ MHz/4096 for the 2012 session and $\Delta\nu_{\mathrm{int}} = 16$ MHz/2048 for the 2014 session were smaller than $\Delta\nu_{\mathrm{diff}}$. Some of our analysis involved further integrations over time and frequency; we will discuss the effect of this in § 7. The values for t_{diff} and $\Delta\nu_{\mathrm{diff}}$ are given for the two sessions in Table 1.

4. INTERFEROMETRIC VISIBILITY

We computed the visibility functions from the prepared cross-spectra. These functions provide the distribution of visibility amplitudes as a function of delay and fringe rate. More specifically, from them we computed the maximum visibility amplitude as a function of projected baseline length, and hence determined the size and characteristics of the scatter-broadened image of the pulsar; and we computed the width of components in the distribution of visibility amplitudes, and thus derived scintillation parameters that describe characteristics of the ISM along the line of sight to the pulsar.

4.1. *Distribution of visibility*

The visibility functions are computed as the inverse Fourier transform of the complex cross-spectra. Although for strong single pulses the visibility amplitudes in the cross spectra had SNR sufficiently high for a useful analysis, we decided to analyze the data from all pulses consistently by using dynamic cross-spectra, or time series of consecutive cross-spectra. We averaged the dynamic cross-spectra over integration times of t_{int} of 100 pulse periods or about 71.4 s. This time is also smaller than t_{diff}.

In Figure 1 we display the 2-dimensional inverse Fourier transform of the dynamic cross-spectrum for a 500-s scan. This is known as the "secondary spectrum," and is displayed as visibility amplitude as a function of delay and fringe rate. The data were obtained on 29 November 2012 in the RCP channel for a projected 200Mλ GBT-SRT baseline. The dis-
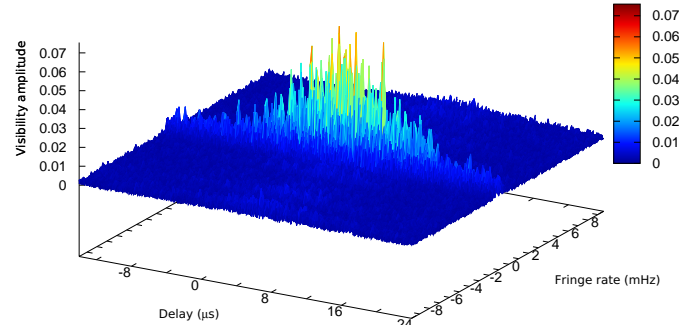

FIG. 1.— Interferometric responce in delay-fringe rate domain for a 500-s scan on 29 November 2012 in the RCP channel on the SRT-GBT baseline.
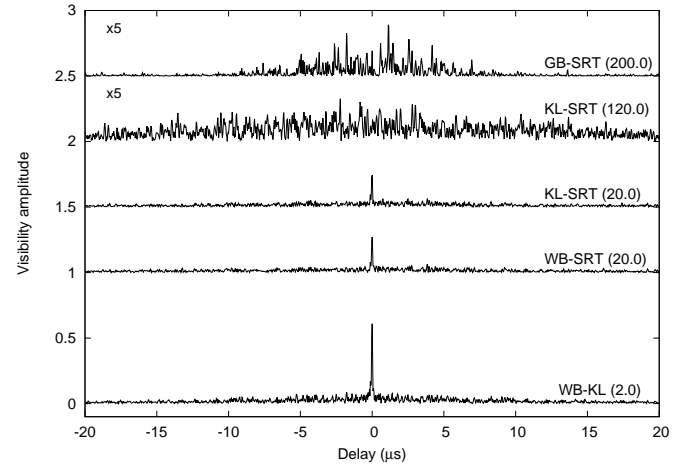

FIG. 2.— Examples of the fine structure of visibility amplitude as a function of delay, with fixed fringe rate, through the maximum of the fringe-rate delay visibility function; in particular, the cross-section of Figure 1 is shown in the uppermost panel. The upper two curves correspond to the longest baseline projections and the lower three curves to shorter baselines, with the telescopes indicated (GB for GBT, WB for WSRT) and the approximate baseline projections given in Mλ in parentheses. The four upper curves are offset by constants for ease of viewing, and the two top curves are, in addition, magnified by a factor 5.

tribution of the visibility amplitudes is relatively broad along the delay axis and relatively narrow along the fringe rate axis.

The distribution of amplitude in the domain of delay and fringe rate changes with baseline length. Figure 2 displays cross-sections through the maximum of the distribution of amplitude, as a function of delay at a fixed fringe rate, close to 0 mHz. The top panel shows the cross-section through Figure 1. The next lower panel shows the cross-section for the slightly shorter SRT-KL baseline. The additional three lower plots give the equivalent cross sections for 10 times and 100 times shorter projected baselines. These three short-baseline cross sections are qualitatively different from the long baseline cross sections: at short baselines the visibility has a central spike resulting from the component of the cross-spectrum that has a constant phase over time, and in addition a broad distribution from the component that has a phase that varies over time. The central spike is strongest for the shortest baseline and weaker for the next longer baselines. At very long baselines the central spike is absent even after averaging the visibility over the whole observing period. On such long baselines only the broad component is present. It consists of isolated spikes distributed over a range of about 10 μs in delay. These spikes keep their position in delay for the scintillation
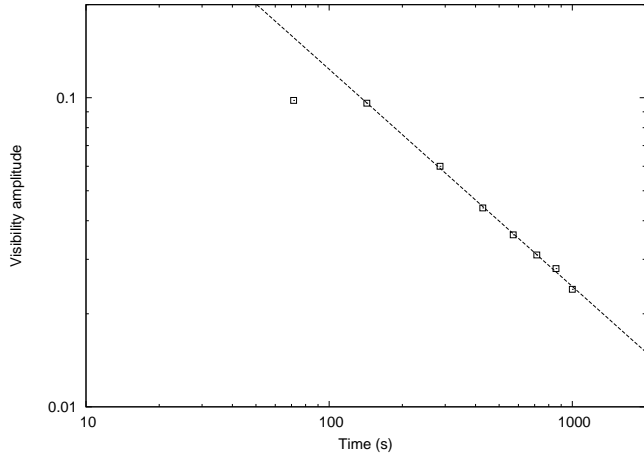
FIG. 3.— Results of calculation of visibility amplitude with increasing integration time for KL-SRT baseline shorter than 30,000 km. Degradation of the visibility amplitude was found to follow the relation $V_{\mathrm{amp}} = 3.14 t_{\mathrm{int}}^{-0.70}$ in the range from 150 to 1000 s of integration.

time of about 100 to 115 s as listed in Table 1.

4.2. *Coherence time*

For our January 2014 observations, we determined the coherence losses as a function of integration time for the cross spectra obtained for the shortest KL-SRT baselines, with projected baseline less than 30,000 km. Figure 3 illustrates the coherence looses as a function of integration time. To obtain the visibility amplitudes as a function of projected baseline length we took the maximum value above the background level in every secondary spectrum obtained for an integration time Δt_{int}. The maxima occurred at residual delays and fringe rates close to zero, with small departures because of relatively small errors in the SRT orbit parameters. For integration times from 150 s to 1000 s the degradation of the visibility amplitude was found to follow the relation $V_{\mathrm{amp}} = 3.14 t_{\mathrm{int}}^{-0.70}$ from which we derived a correction factor for visibility amplitudes of 2.50, which we applied to correct data obtained in November 2012.

4.3. *Averaged maximum visibility amplitudes*

Our selection of the fringe-rate peak implies an effective integration time. For our November 2012 observations, this implied integration time is $\Delta t_{\mathrm{int}} = 500$ s. Hence, for our November 2012 observations, $\Delta t_{\mathrm{int}} > t_{\mathrm{diff}}$, so that coherence losses occurred and the visibility amplitudes needed to be corrected. For the January 2014 observing session each secondary spectrum was computed over 100 pulsar periods ($\Delta t_{\mathrm{int}} = 71.4$ s), short enough so that no coherence losses were expected and no correction for it needed to be applied. The visibility amplitudes were taken as the maxima from the secondary spectra, and then averaged for every 16×100 pulsar periods, that is for 1170 s. These maximum visibility amplitudes for the November 2012 and January 2014 sessions give information about the scatter broadened image of the pulsar, by providing the fringe amplitude as a function of baseline length.

4.4. *Normalized visibility amplitudes*

To obtain information about the scatter-broadened image of the pulsar, we normalized the averaged visibility amplitudes. To obtain these amplitudes we analyzed the secondary spectra in more detail. We found that the central spike takes the form
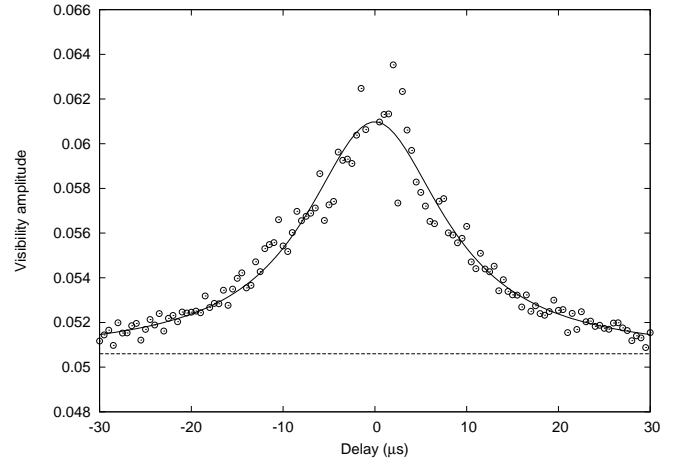

FIG. 4.— Cross-section of a secondary spectrum along the delay axis, at the fringe rate where the visibility amplitudes peaked, close to zero mHz. The visibility amplitudes are shown as open circles for the broad component without the narrow central component for the KL-SRT baseline. Visibilities were computed in 71.4 s time intervals but averaged over an observing scan of 1170 s, and then further averaged over 16 points or 0.5 μs in delay to smooth fluctuations. The Lorentzian fit function (solid line) above the background level (dashed line) is also shown.

of a sinc function in both delay and fringe rate coordinates. The broader distribution takes that of a Lorentzian along the delay coordinate, and of an exponential function along the fringe rate coordinate for individual scans. We do not analyze the broad distribution in fringe rate here further; we will discuss this distribution, and the influence of traveling ionospheric disturbances, in a separate publication. We used the functional form along the delay axis to fit the central spike and the broad component. The fit also included parameters for the background noise level. We made this fit near zero fringe-rate at the peak of the visibility amplitude in the secondary spectrum. An example of a fit of the broad component with a Lorentzian, above the background noise level, is given in Figure 4.

To find the normalized amplitude of visibility, we computed the area under the sinc function fit to the narrow central component, P_n, and the area under the Lorentzian fit to the broad distribution, P_b. We normalized the values by setting $P_n + P_b \equiv 1$ μs = const. The "normalized average visibility" $R = P_n/(P_n + P_b)$ is then another variable that depends on the baseline length and can be used to determine the size of the scattering disk. However, meaningful values were only determined for the shorter baselines for which a central spike was clearly visible. Information about the scattering disk on the long baselines could only be obtained from the maximum visibility amplitudes described earlier. The maximum visibility amplitudes and the normalized average visibility, R, and their behavior as a function of projected baseline length, are described further in § 5.

4.5. *Width of visibility distribution*

Our fits of the sinc function and the Lorentzian to the distribution of visibility amplitude in the secondary spectrum determined the widths of these components. In Table 1 we list the fit half-width at half maximum (HWHM) of the narrow central component in delay, $w_{n\tau}$, and in fringe rate, w_{nf}, and of the broad component in delay, $w_{b\tau}$. The width of the broad component is the time broadening of a sharp pulse, from scattering. We found no dependence of the widths on projected
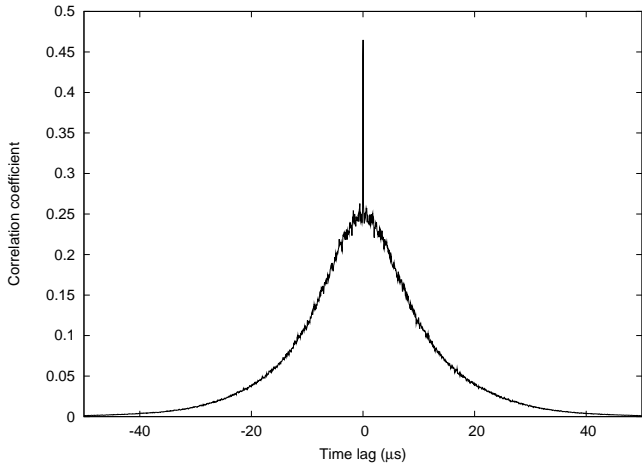
Fɪɢ. 5.— Delay cross-section at zero fringe rate of the two-dimensional CCF between RCP and LCP secondary spectra obtained on the GBT-SRT baseline for a 500-s observing scan on 26 November 2012. The projected baseline is 60 Mλ.

baseline length. We discuss these widths in terms of the distance of the scattering material from Earth along the line of sight to the pulsar in § 6.

4.6. *Cross-correlation of secondary spectra*

The broad Lorentzian peak shown in Figure 4 is composed of fine structure as Figure 2 shows. To obtain information about this fine structure, we computed the two-dimensional cross-correlation function (CCF) between the right-circular polarized (RCP) and left-circular polarized (LCP) secondary spectra. In contrast to the autocorrelation functions (ACF) of either RCP or LCP secondary spectra, the CCF has no spike of correlated noise at the origin. Any such spike would have to be attributed to the pulsar. We selected spectra obtained with an integration time of 500 s on 26 November 2012. The projected baseline length was 60 Mλ, not as long as the longest baselines in Figure 2, but long enough that only fine structure and the broad component appeared. The central part of the CCF will therefore measure properties of the fine structure, while the broad part will measure properties of the broad component.

As expected, two components can be distinguished: a narrow spike near the origin that characterizes the fine structure, and a broad component that characterizes the Lorentizan. To illustrate these components clearly, Figure 5 shows the cross-section of the 2-dimensional cross-correlation function as a function of delay at zero fringe rate. We measured the half-width at half-maximum (HWHM) of the narrow spike in delay by fitting a sinc function and found $w_{n\tau,\mathrm{CCF}} = 36 \pm 2$ ns. We measured the HWHM in fringe rate by fitting an exponential function and found $w_{nf,\mathrm{CCF}} = 1.4 \pm 0.1$ mHz. These two values measure the typical width in delay and fringe rate of the fine structure. They should not be confused with the widths of the central spike on the short baselines $w_{n\tau}$ and w_{nf} (see Figure 2). We measured the HWHM of the broad component in delay by fitting a Gaussian to find $w_{b\tau,\mathrm{CCF}} = 5.8 \pm 0.2$ μs. As expected, this value is in approximate agreement with the value of $w_{b\tau}$ obtained by fitting a Lorentzian distribution to the visibility functions (see Table 1). As for the secondary spectra, we do not further analyze the broad component in fringe rate. Again, we did not find any dependence of the fitted widths on the length of the projected baseline. The narrow spike and the broad component give information about the na-
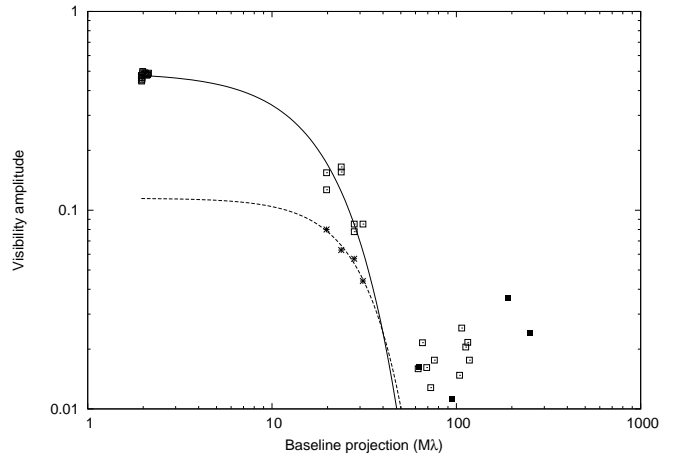

Fɪɢ. 6.— Visibility amplitude versus projected baseline length. The maximum visibility amplitudes are plotted for the November 2012 session as black squares and for the January 2014 session as open squares. All of the points were averaged for 16000 pulsar periods. The solid line shows the fit to the data on the short baselines with equation (3), corresponding to a scattering disk size $\theta_{\mathrm{H}} = 5.2$ mas. The normalized average visibilities, R, for the January 2014 session, are plotted as stars. The dashed line shows the fit to the data with the same equation, corresponding to a disk size $\theta_{\mathrm{H}} = 4.2$ mas.

ture of the pulses, as we elaborate upon in § 8.

5. THE SCATTER BROADENED IMAGE OF THE PULSAR AND SUBSTRUCTURE WITHIN IT

To obtain information on the size and characteristics of the scatter-broadened image of the pulsar, we plot the maximum and normalized average of the visibility amplitudes as a function of projected baseline length, b, in Figure 6. The figure shows four groups of points: maximum visibility amplitudes on short ground-ground baselines ($b \sim 2000$ km), on intermediate ground-space baselines ($b \sim 15,000$ to $20,000$ km), and on the longest ground-space baselines ($b \sim 60,000$ to $235,000$ km); and normalized average visibility, R, on intermediate ground-space baselines.

Each of the four groups of points shows internal scatter. We argue that this scatter does not arise from noise, but rather from variation of the scintillation on timescales much longer than t_{diff}. For example, for the first group observed in the January 2014 session, on the shortest baselines the root mean square variation of 100-pulsar-period maximum visibility amplitudes is 0.06 (11%). Increasing the integration time by a factor of 16 decreases the root-mean-square by a factor of four, to 0.015 (3%), as would be expected for random noise-like variations. We find the same relative rms values of 3% for the second and third groups. For each of the three groups the relative rms values are smaller than the size of the symbols. Therefore, we argue that the scatter is not the result of statistical noise, but from longer-term variations.

The expected visibility amplitude due to angular broadening is given by Gwinn et al. (1988) as

$$V_{AB} = \exp\left(-\frac{1}{2}\left(\frac{\pi}{(2\ln 2)^{1/2}}\frac{\theta_{\mathrm{H}} b}{\lambda}\right)^{\alpha-2}\right) \qquad (3)$$

with, e.g., $\alpha = 4$, for a Gaussian. The parameter, α, is the spectral index of density fluctuations and, b, the projected baseline length of the interferometer, θ_{H} is the full width at half maximum (FWHM) diameter of the scattering disk. Clearly, this function can not provide a good fit to the maximum visibility amplitudes on all baselines. Only those on the short and inter-

mediate baselines provided a good fit, with the fitting function shown as a solid line. We obtained for the maximum visibility amplitudes, plotted with open squares, $\theta_H = 5.2 \pm 0.4$ mas, and $\alpha = 3.5 \pm 0.1$ with uncertainties as formal errors. For the normalized average visibility amplitudes, R, plotted with stars, we obtained $\theta_H = 4.2 \pm 0.4$ mas, for a range of fixed values for α with $\alpha = 3.5$ giving the smallest χ-squared per degree of freedom. The values of θ_H agree with each other within a relatively small discrepancy of 1.8σ. We take the mean value $\theta_H = 4.7 \pm 0.9$ mas for our subsequent analysis, with the error comprising the 1σ errors of each of our two measurements. The power-law index α for PSR B0329+54 was also measured by Shishov et al. (2003) in their multi-frequency study; they found $\alpha = 3.50 \pm 0.05$ in good agreement with our result.

Our fit functions fall toward zero very rapidly for baselines longer than $\sim$60 Mλ. At the longest earth-space baselines, the models are many orders of magnitude smaller than the visibility amplitudes we measured. For baselines from 60 to 235 Mλ, our observations are scattered around a mean of $\sim$0.04 of the maximum at $\sim$zero baseline. This indicates structure on very small scales that equation (3) cannot describe. Clearly the scatter-broadened image of PSR B0329+54 is resolved, and substantial substructure exists in it.

6. THE SCATTERING MATERIAL IN THE ISM ALONG THE LINE OF SIGHT TO THE PULSAR

PSR B0329+54 is located at the outer edge of the Orion spiral arm, whereas the Sun is close to the inner edge of the arm. A comparison of angular and temporal broadening provides information on the distribution of the scattering material in this arm along the line of sight to the pulsar. Expressions for the angular diameter θ_H and the broadening time τ_{scat} have been derived by Blandford & Narayan (1985). These expressions contain the function $\psi(z)$ which defines the mean scattering angle per unit length, z, measured from the source to the observer.

For the simple case, where the scattering material is uniformly distributed along the line of sight to the pulsar, $\psi(z)$ is a constant, and $\theta_H^2 = 16 \ln 2 (c\tau_{\text{scat}}/D)$ (Britton et al. 1998), with D being the distance to the pulsar. This relation gives for our values of the broadening time, $\tau_{\text{scat}} = w_{b,\tau}$ of 5.1 ± 0.2 μs and 7.5 ± 0.5 μs, values of $\theta_H = 4.8 \pm 0.7$ mas and 5.8 ± 0.8 mas for the November 2012 and January 2014 sessions, respectively, with the errors including those for D. For the November 2012 session our baselines were too long for a measurement of θ_H but for the January 2014 session the above theoretically predicted value could be compared with our measurement of the mean value of $\theta_H = 4.7 \pm 0.9$ mas. They agree within 1σ. Therefore, for this relatively simple case, a model of uniformly distributed scattering material along the line of sight to the pulsar would be in agreement with our result.

For another simple case where the scattering material is only distributed in a thin screen located at a distance d_{scr} from Earth, $\theta_H^2 = 8 \ln 2 c\tau_{\text{scat}}(\frac{D-d_{\text{scr}}}{Dd_{\text{scr}}})$ (Britton et al. 1998). This relation gives us for our measured values of θ_H and τ_{scat} from the November and January sessions, $d_{\text{scr}} = (0.33 \pm 0.12)D$ and $d_{\text{scr}} = (0.43 \pm 0.12)D$, respectively, with a mean value of $d_{\text{scr}} = (0.38 \pm 0.17)D$.

A different relation between θ_H and the distances, D and d_{scr}, can be also considered. This relation includes the diffractive scintillation time, t_{diff}, the associated diffractive length-scale, r_{diff}, in the plane of the observer normal to the line of sight to the pulsar, and the velocity of the scintillation pattern

with respect to the observer, v_{diff}, with

$$r_{\text{diff}} = v_{\text{diff}} t_{\text{diff}}. \tag{4}$$

The velocity, v_{diff}, is a geometrical function of the velocities of the observer, v_{obs}, the scattering screen, v_{scr}, and the pulsar, v_{psr}, as well as the distances, D and d_{scr}, and is given by

$$v_{\text{diff}} = v_{\text{obs}} - \frac{D}{d_{\text{scr}}} v_{\text{scr}} + \frac{D-d}{d_{\text{scr}}} v_{\text{psr}}. \tag{5}$$

We estimated r_{diff} by comparing the expression for the visibility amplitude versus baseline (Prokhorov et al. 1975; Goodman & Narayan 1989):

$$V_{AB} = \exp\left(-\frac{1}{2}\left(\frac{b}{r_{\text{diff}}}\right)^{\alpha-2}\right) \tag{6}$$

with equation (3). We obtained

$$r_{\text{diff}} = \left(\frac{\lambda}{\theta_H \pi}\right)\sqrt{2\ln 2} \tag{7}$$

and $r_{\text{diff}} = (1.5 \pm 0.3) \times 10^4$ km, with the error reflecting the error of θ_H.

With r_{diff} and t_{diff} determined, v_{obs} and v_{psr} known and v_{scr} assumed to be in the range of 0–15 km s^{-1}, we get for the November and January session values, $d_{\text{scr}} = (0.34 \pm 0.10)D$ and $(0.37 \pm 0.09)D$, respectively, with a mean of $d_{\text{scr}} = (0.35 \pm 0.10)D$, thus placing the effective scattering screen at a distance of about one third away from Earth toward the pulsar.

7. INTERPRETATION OF THE SUBSTRUCTURE IN THE SCATTER-BROADENED IMAGE OF PSR B0329+54

The diffraction scatter-broadened image of PSR B0329+54 with angular size, θ_H, is reflected in the rapidly decaying visibility amplitudes up to $b \sim 40$ Mλ. For longer baselines the image should be completely resolved and no visiblity detected, as indicated by the fitting function 3. However, visibility is indeed detected. The amplitude varies, but remains approximately constant up to the longest observed baselines of about 250 Mλ. Further, as shown in Figure 2, the cross-sections of the secondary spectra are qualitatively different for different baselines. For shorter baselines, the cross-sections consist of a broad component and a central narrow spike, whereas for long baselines the central narrow spike disappears. How can that be understood?

General aspects of the ground-space interferometer and the scattering medium present important considerations for substructure. For radio waves through the ISM, scattering is considered to be strong, meaning that the lengths of the many paths the scattered radio waves take from the pulsar to the observer differ by many wavelengths. Goodman & Narayan (1989) and Narayan & Goodman (1989) distinguished three cases for strong scattering: snapshot, average, and ensemble-average regimes. Of these, two are relevant to our space VLBI data, the snapshot and the average regime. In the snapshot regime, the relative phases of the radio waves travelling along different paths remain mostly unchanged during the observations. The interferometer observes a pattern of speckles whose parameters are a function of the size of the source and of small and large-scale electron density variations in the ISM. In the average regime, some averaging over several different paths smooths effects of small-scale density variations to zero, leaving only the visibility from the large-scale variations in action. In the ensemble-average regime, all variations

are smoothed out, leaving only a smooth visibility function like that given by equation (3). The averaging that carries an observation from one regime to the next may be accomplished by time averaging, frequency averaging, or averaging over finite source size.

For our observations, the size of the source is very small. Pulsar radio emission is generated in a very compact region inside the magnetosphere of a neutron star. Even if the size of the emission region is as large as the light cylinder, the angular size of that region for PSR B0329+54 would be only 2.3×10^{-12} rad or 0.5 μas, smaller than 0.001 times the angular resolution of VLBI with *RadioAstron* on any baseline. Therefore, pulsars are essentially "point-like" radio sources and all signatures of the visibility data are therefore due to the small and large-scale density variations in the ISM. Further, the averaging of our cross spectra over 100 pulse periods or 71.4 s, is less than t_{diff} and therefore small enough to be in the so-called snapshot regime where no damping of visibility amplitudes is expected. However, the receiver bandwidth, $\Delta\nu_{\mathrm{int}} = 16$ MHz is much larger than the scintillation bandwidth $\Delta\nu_{\mathrm{diff}} \sim 7$ to 15 kHz, resulting in a decrease of the visibility amplitudes.

In our observations the b/r_{diff} ratio varies from 0.1 to about 15. For a small ratio up to about 1, the projected baseline was small and the corresponding beam size of the interferometer large enough to average over many paths the scattered radio waves took from the pulsar to Earth. The ground telescopes and the SRT were still within a single diffraction spot. This is the average regime where the visibilities from any possible small-scale density variations of the ISM were averaged to zero and only those from large-scale density variations survived. On these baselines our interferometer only measured the scatter-broadened image of the pulsar. For larger ratios of b/r_{diff} up to 15, the two telescopes were not in the same diffraction spot anymore. The scatter-broadened image was completely resolved resulting in essentially zero visibility from the smooth, ensemble-average scattering disk. However, in the snapshot regime, substructure can still arise from diffractive scintillation. Even on an arbitrarily long baseline, for point-like emission, diffractive scintillation results in a stochastic visibility that decorrelates over scales of $\Delta\nu_{\mathrm{diff}}$ and t_{diff} (Johnson & Gwinn 2013). Substituting our parameters, we expect long-baseline amplitudes of order $\sim (\Delta\nu_{\mathrm{diff}}/\nu_{\mathrm{int}})^{1/2} \approx 3\,\%$ relative to the zero-baseline limit. Thus, our measurements and their variation are compatible with the expected visibility contribution from diffractive scintillation. Extended sources, such as SgrA*, that quench the diffractive scintillation can more readily reveal the refractive contribution to substructure (see Gwinn et al. 2014). Clearly, substructure in the scatter-broadened image of PSR B0329+54 was detected, most likely due to small-scale electron density fluctuations in the ISM.

8. INTERPRETATION OF THE SUBSTRUCTURE IN TERMS OF AN AMPLITUDE-MODULATED NOISE MODEL

A simple model, similar to amplitude-modulated noise (AMN), explains the form of the CCF of the secondary spectrum. As discussed in § 4.6 and shown in Figure 4, the CCF shows a narrow spike on top of a broad component. The narrow spike corresponds to many isolated unresolved spikes in the secondary spectra, and the broad component to the overall scale of the secondary spectrum, which in turn is set by temporal broadening.

Rickett (1975) used an analogous model to explain microstructure properties in pulsar radio emission. In their model the observed electric field $E(t)$ is the product of a real amplitude modulation $a(t)$ and a complex stationary noise process, $n(t)$:

$$E(t) = a(t)n(t) . \qquad (8)$$

The noise $n(t)$ is assumed to be uncorrelated, stationary, and white; and drawn from a Gaussian distribution in the complex plane. Consequently, the intensity is the product of an amplitude factor $a^2(t)$, and an uncorrelated, stationary, random process $\epsilon(t) = |n(t)|^2$ drawn from an exponential distribution:

$$I(t) = a^2(t)\epsilon(t) . \qquad (9)$$

Of course, $a(t)$ and $\epsilon(t)$ are assumed to be uncorrelated. Note that, for an exponential distribution,

$$A_\epsilon \equiv \langle \epsilon^2 \rangle = 2 \left(\langle \epsilon \rangle \right)^2 . \qquad (10)$$

The peak of the ACF of intensity lies at a lag of zero:

$$ACF(0) = \tfrac{1}{T}\sum_t I(t)^2 = \tfrac{1}{T}\sum_t a^4(t)\epsilon(t)^2 = \\ \langle a^4 \rangle \langle \epsilon^2 \rangle = A_a \cdot A_\epsilon , \qquad (11)$$

where we define $A_a \equiv \langle a^4 \rangle$. One lag away from the peak, the value of the ACF is:

$$ACF(1) = \tfrac{1}{T}\sum_t I(t)I(t+1) = \\ \tfrac{1}{T}\sum_t a^2(t)a^2(t+1)\epsilon(t)\epsilon(t+1) = \\ \langle a^4 \rangle \left(\langle \epsilon \rangle \right)^2 \approx A_a \cdot \tfrac{1}{2}A_\epsilon , \qquad (12)$$

where we assume that $a(t+1) \approx a(t)$. This is one of the tests of the AMN model: that the maximum of the broad distribution (at about one lag from the maximum of the entire distribution) has half the maximum of the entire distribution.

We correlate $|V|$, the amplitude of the complex visibility, V, in the lag/fringe-rate domain, between left and right circular polarization. We suppose that this visibility is the product of a rapidly-varying, uncorrelated noise, $b(t)$, that describes the narrow spikes, and a slowly-varying envelope, $a(t)$, that describes the overall scale of the secondary spectrum: In our model, the complex visibility, $V(f)$, in the fringe-rate is the product of an amplitude factor, $a(f)^2$, and a stationary, uncorrelated random process $b(f)$:

$$V(f) = a^2(f)b(f) . \qquad (13)$$

Here, the amplitude a^2 characterizes the variation of the secondary spectrum because of temporal broadening. The random variable $b(f)$ is drawn from an uncorrelated, stationary, complex distribution.

Analogously to the the AMN model, the peak of the CCF of visibility lies at a lag of zero:

$$CCF(0) = \tfrac{1}{T}\sum_t |V(t)|^2 = \tfrac{1}{T}\sum_t a^4(t)|b(t)|^2 = \\ \langle a^4 \rangle \langle |b|^2 \rangle = A_a \cdot A_b , \qquad (14)$$

where we define $A_b \equiv \langle |b|^2 \rangle$. One lag away from the peak, the value of the CCF is:

$$CCF(1) = \tfrac{1}{T}\sum_t |V(t)| \, |V^*(t+1)| = \\ \tfrac{1}{T}\sum_t a^2(t)a^2(t+1)|b(t)| \, |b(t+1)| = \\ \langle a^4 \rangle \left(\langle |b| \rangle \right)^2 , \qquad (15)$$

where we again assume that $a(t+1) \approx a(t)$, and recall that $a(t)$ is real. We conclude that the ratio of the height of the peak of

the broad plus narrow components, to the height of the broad component only, is

$$\frac{CCF(0)}{CCF(1)} = \frac{\langle |b|^2 \rangle}{\left(\langle |b| \rangle\right)^2} . \qquad (16)$$

Our observations indicate that this ratio has the value 1.9, as Figure 4 shows. This is in approximate agreement with the prediction of 2.0 for an exponential distribution of b. By contrast, a Rayleigh distribution for b produces a ratio of $16/\pi^2$, whereas a distribution of the irregular Bessel function of the second kind of order 0, K_0, appropriate for the product of elements from 2 uncorrelated complex Gaussian distribution, yields a ratio of 2.47 (Gwinn 2001).

9. SUMMARY

We made VLBI observations of PSR B0329+54 with *RadioAstron* at 324 MHz on projected baselines of up to 235,000 km. Our goal was to investigate scattering properties of the ISM. These properties affect radio observations of all celestial sources. While the results of such observations are in general influenced by the convolution of source structure with the scattering processes, pulsars are virtually point-like sources and signatures in the observational results can be directly related to the ISM scattering properties.

The scattering disk of PSR B0329+54 was completely resolved on ground-space baselines longer than about 30,000 km. The FWHM of the angular diameter is 4.7 ± 0.9 mas. The diffractive length scale or size of the diffraction spot near Earth is $15,000 \pm 3,000$ km. With the assumption of turbulent and large-scale irregularities in the plasma, the effective scattering screen is located 0.35 ± 0.10 or at about a third of the distance from Earth to the pulsar.

At projected baselines of 60,000 to 235,000 km, we detected significant visibility amplitudes, although none were expected from the smooth scattering disk. They vary around a mean of about 0.04 of maximum visibility at zero baseline, and remain constant up to the longest baselines. This is the first time interferometric detections have been obtained from a completely resolved scatter-broadened image where the source is quasi point-like and the detections fully attributible to the properties of the interstellar medium. This detection represents the discovery of substructure in the scatter-broadened image of PSR B0329+54. The discovery is confirmed and complemented by similar findings towards SgrA* (Gwinn et al. 2014). The autocorrelation function of the visibility in delay corresponds to the model of amplitude-modulated noise, indicating that visibility spikes are the result of random interferences of many scattered rays.

REFERENCES

Alexandrov, Y. A., Andreyanov, V. V., Babakin, N. G., et al. 2012, Solar System Research, 46, 466
Bartel, N., Ratner, M. I., Shapiro, I. I., et al. 1985, AJ, 90, 2532
Blandford, R., & Narayan, R. 1985, MNRAS, 213, 591
Brisken, W. F., Benson, J. M., Goss, W. M., & Thorsett, S. E. 2002, ApJ, 571, 906
Britton, M. C., Gwinn, C. R., & Ojeda, M. J. 1998, ApJ, 501, L101
Desai, K. M., Gwinn, C. R., Reynolds, J., et al. 1992, ApJ, 393, L75
Edwards, R. T., Hobbs, G. B., & Manchester, R. N. 2006, MNRAS, 372, 1549
Goodman, J., & Narayan, R. 1989, MNRAS, 238, 995
Gwinn, C. R. 2001, ApJ, 554, 1197
Gwinn, C. R., Bartel, N., & Cordes, J. M. 1993, ApJ, 410, 673
Gwinn, C. R., Bartel, N., Cordes, J. M., Wolszczan, A., & Mutel, R. L. 1988, ApJ, 334, L13
Gwinn, C. R., Britton, M. C., Reynolds, J. E., et al. 1998, ApJ, 505, 928
Gwinn, C. R., Kovalev, Y. Y., Johnson, M. D., & Soglasnov, V. A. 2014, ApJ, 794, L14
Haslam, C. G. T., Salter, C. J., Stoffel, H., & Wilson, W. E. 1982, A&AS, 47, 1

Johnson, M. D., & Gwinn, C. R. 2013, ApJ, 768, 170
Kardashev, N. S., Khartov, V. V., Abramov, V. V., et al. 2013, Astronomy Reports, 57, 153
Kondratiev, V. I., Popov, M. V., Soglasnov, V. A., et al. 2007, Astronomical and Astrophysical Transactions, 26, 585
Kovalev, Y. A., Vasil'kov, V. I., Popov, M. V., et al. 2014, Cosmic Research, 52, 393
Narayan, R., & Goodman, J. 1989, MNRAS, 238, 963
Pence, W. 1999, in Astronomical Society of the Pacific Conference Series, Vol. 172, Astronomical Data Analysis Software and Systems VIII, ed. D. M. Mehringer, R. L. Plante, & D. A. Roberts, 487
Prokhorov, A., Bunkin, V. F., Gochelashvily, K. S., & Shishov, V. I. 1975, Proc. IEEE, 63, 790
Rickett, B. J. 1975, ApJ, 197, 185
—. 1977, ARA&A, 15, 479
Shishov, V. I., Smirnova, T. V., Sieber, W., et al. 2003, A&A, 404, 557
Yangalov, A. K., Popov, M. V., Soglasnov, V. A., et al. 2001, Ap&SS, 278, 39